Eidgenössische Technische Hochschule Zürich

Ecole polytechnique fédérale de Zurich
Politecnico federale di Zurigo
Swiss Federal Institute of Technology Zurich

Solution of the $3D$-Helmholtz equation in exterior domains of arbitrary shape using HP-finite infinite elements

K. Gerdes

Research Report No. 96-21
December 1996

Seminar für Angewandte Mathematik
Eidgenössische Technische Hochschule
CH-8092 Zürich
Switzerland

Solution of the $3D$-Helmholtz equation in exterior domains of arbitrary shape using HP-finite infinite elements

K. Gerdes

Seminar für Angewandte Mathematik
Eidgenössische Technische Hochschule
CH-8092 Zürich
Switzerland

Research Report No. 96-21 December 1996

Abstract

This work is devoted to a convergence and performance study of finite-infinite element discretizations for the Helmholtz equation in exterior domains of arbitrary shape. The proposed approximation applies to arbitrary geometries, combining an *hp* FE discretization between the object and a surrounding sphere and an *hp* Infinite Element (IE) discretization outside the sphere with a spectral-like representation (resulting from the separation of variables) in the "radial" direction. The described approximation is an extension of our earlier work, which was restricted to domains with separable geometry. The numerical experiments are confined to these geometrical configurations: a sphere, a (finite) cylinder, and a cylinder with spherical incaps, all within a truncating sphere. The sphere problem admits an exact solution and serves as a basis for the convergence study. Solutions to the other two problems are compared with those obtained using the Boundary Element Method.

1 Introduction

The presented paper is motivated by our earlier work on elastic scattering (see [9] for the latest results) and the new concept on various infinite elements by Burnett [4], Astley et all [1], Cremers et all [5] and our own work [13, 8].

The eventual problem of interest deals with scattering of acoustic waves on elastic or rigid (the simplified case) objects. The mathematical formulation consists of the Helmholtz equation in the exterior domain accompanied by the Sommerfeld radiation condition and Neumann boundary condition on the boundary of the scatterer (rigid scattering). In the elastic scattering case, the Helmholtz equation is coupled to equations describing behavior of the structure (elasto- or viscoelasto-dynamics). The presented work discusses the rigid scattering case only.

Problems of the described type are usually solved using various versions of the Boundary Element Method (BEM). The mathematics of the BE approximation (especially in the Galerkin version) is well established and the method delivers reliable results in the whole range of wave numbers. The main drawback of the BEM is its cost - the method becomes prohibitively expensive for large wave numbers.

The approach based on the truncation of the infinite domain to a finite one and application of the so called *open boundary* conditions has always been an alternative technique to solve the problem. In particular, the recent versions of the Infinte Elements based on multipole expansions seem to be especially attractive as they offer accuracy of arbitrary high order and can be coupled with standard C^0 finite elements. The recent results on convergence of such methods [2, 8] support reliability of such an approach and add to its attractiveness.

The common property of the methods presented in [4, 1, 5] is that both approaches use a variable number of basis functions in the radial direction. The essential difference appears in the underlying variational formulations (though never explicitly stated in [4, 1, 5]). The scheme proposed in [1, 5] is based on a formulation in weighted Sobolev spaces and consistent with the existence and uniqueness theory by Leis [16]. This is also the approach which we investigated in [13] and continue to use in this work. The concept presented in [4] is based on a different variational formulation, also shortly discussed in [13].

Another essential difference between the various versions of the infinite elements has been recently pointed out in [2]. The difference lies in the fact whether one *does* or *does not* use the complex conjugate over the test functions (sesquilinear vs. bilinear form formulation).

In the presented approach we couple the standard FEM with the IEM, based on the Leis sesquilinear variational formulation. The scatterer is surrounded with a truncating sphere. In between the scatterer and the truncating sphere we use 3D *hp*-FE approximations described in [9]. Outside the sphere, the compatible *hp*-discretization on the sphere is combined with a spectral like approximation in the radial direction.

Numerical results are confined to these geometries: a sphere, a (finite) cylinder and a (finite) cylinder with spherical incaps. The sphere problem admits an exact solution which is used to compute the convergence rates. The numerical solutions to the cylinder problems are compared with solutions obtained by the BEM discussed in [9].

The plan of the presentation is as follows. We begin by formulating the Helmholtz equation and describing the IE in section 2. Numerical experiments are presented in section 3. Section 4 discusses some preliminary results on a-posteriori error estimation and *hp*-adaptivity, and we finish the presentation with concluding remarks in section 5.

2 Coupled FE/IE Discretizations for the Helmholtz Equation in Arbitrary Exterior Domains

2.1 Notation

- $\Omega \subset \mathbb{R}^3$ is a domain occupied by the rigid scatterer and contained in the unit sphere
- $\Omega^e = \mathbb{R}^3 - \Omega$ is the domain exterior to the scatterer
- $\Gamma_s = \{\boldsymbol{x} \in \mathbb{R}^3; |\boldsymbol{x}| = 1\}$ is the surface of the unit sphere
- $\Omega_s^e = \{\boldsymbol{x} \in \mathbb{R}^3; |\boldsymbol{x}| > 1\}$ is the domain exterior to the unit sphere
- $\Gamma = \partial\Omega$ is the surface of the rigid scatterer
- $\Omega_s = \{\boldsymbol{x} \in \mathbb{R}^3; |\boldsymbol{x}| \leq 1\} - \Omega$ is the domain between the unit sphere and the rigid scatterer

The notation is illustrated in Figure 1.

2.2 Classical Formulation of the Problem

The goal is to find a function $u = u(\boldsymbol{x})$ satisfying:

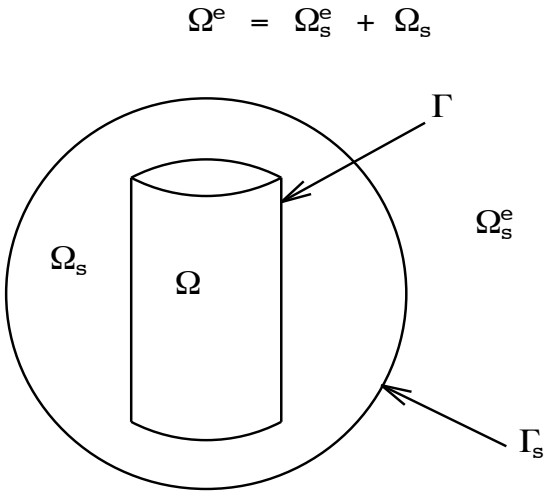

Figure 1: Notation. Cylinder within a unit sphere.

- the Helmholtz equation in the domain exterior to the scatterer,

$$-\Delta u - k^2 u = 0 \qquad \text{in} \quad \Omega^e \tag{2.1}$$

  where k is the wave number;

- a Neumann boundary condition on the scatterer

$$\nabla_n u = \tilde{g} \qquad \text{for} \quad \boldsymbol{x} \in \Gamma \tag{2.2}$$

  where $\tilde{g}$ is a prescribed function on Γ;

- the Sommerfeld radiation condition at infinity,

$$\left| \frac{\partial u}{\partial n} - iku \right| = O\left(\frac{1}{r^2}\right) \tag{2.3}$$

2.3 Variational Formulation and Existence Theory

Given a "truncated" exterior domain Ω_γ^e,

$$\Omega_\gamma^e = \Omega^e \cap \left\{ \boldsymbol{x} \in \mathbb{R}^3 \,:\, |\boldsymbol{x}| < \gamma \right\}$$

the Helmholtz equation is multiplied by the complex conjugate of a test function v, integrated over the truncated domain Ω_γ^e, and integrated by parts. Using the Neumann

boundary condition on $\partial\Omega^e_\gamma$ results in the following equation, for any admissible test function v,

$$\int_{\Omega^e_\gamma} \boldsymbol{\nabla} u \cdot \boldsymbol{\nabla} \overline{v}\, d\Omega^e_\gamma - k^2 \int_{\Omega^e_\gamma} u\, \overline{v}\, d\Omega^e_\gamma - \int_{S_\gamma} \frac{\partial u}{\partial n} \overline{v}\, dS_\gamma = \int_\Gamma \tilde{g}\, \overline{v}\, dS \tag{2.4}$$

where S_γ is the "truncating" sphere with radius $r = \gamma$. Rewriting the Sommerfeld radiation condition (2.3) in the form

$$\frac{\partial u}{\partial r} = iku + \varphi(\boldsymbol{x}) \tag{2.5}$$

where $\varphi(\boldsymbol{x}) = O\left(r^{-2}\right)$ is an *unknown* function, and building it into the variational formulation (2.4) by substituting for $\partial u/\partial n = \partial u/\partial r$ in the corresponding boundary term formula (2.5), we get

$$\int_{\Omega^e_\gamma} \boldsymbol{\nabla} u \cdot \boldsymbol{\nabla} \overline{v}\, d\Omega^e_\gamma - k^2 \int_{\Omega^e_\gamma} u\, \overline{v}\, d\Omega^e_\gamma - ik \int_{S_\gamma} u\overline{v}\, dS_\gamma = \int_{\partial\Omega^e} \tilde{g}\, \overline{v}\, dS + \int_{S_\gamma} \varphi\overline{v}\, dS_\gamma \tag{2.6}$$

Passing formally with $\gamma \to \infty$, we obtain

$$\begin{aligned} & \int_{\Omega^e} \boldsymbol{\nabla} u \cdot \boldsymbol{\nabla} \overline{v}\, d\Omega^e - k^2 \int_{\Omega^e} u\, \overline{v}\, d\Omega^e - ik \lim_{\gamma\to\infty} \int_{S_\gamma} u\overline{v}\, dS_\gamma \\ = & \int_\Gamma \tilde{g}\, \overline{v}\, dS + \lim_{\gamma\to\infty} \int_{S_\gamma} \varphi\overline{v}\, dS_\gamma \end{aligned} \tag{2.7}$$

From a general theory in [16, 19], it is known that the leading order term of $u|_{\Omega^e_s}$ is of the form

$$u_0(\boldsymbol{x})\, \frac{\exp(ikr)}{r}\,, \qquad \boldsymbol{x} \in \Gamma_s$$

and, consequently, both u and its gradient, $\boldsymbol{\nabla} u$, are *not* L^2-integrable over the exterior domain, similarly as for the sphere problem. A remedy to this problem is again to employ different test functions in Ω^e_s, of order $O\left(r^{-3}\right)$. This makes it possible to interprete the integrals in the usual Lebesgue sense. As for the sphere problem, this particular choice of the test functions *does not* allow one to build the radiation condition into the weak formulation, and the Sommerfeld condition has to be included directly in the definition of the spaces. This leads to the definition of the following weighted Sobolev space

$$H^+_{1,w}(\Omega^e_s) = \left\{ u : \|u\|^+_{1,w} < \infty \right\} \tag{2.8}$$

with the norm $\|u\|^+_{1,w}$ corresponding to the inner product

$$(u, v)^+_{1,w} = \int_{\Omega^e} w\, u\, \overline{v} + w\, \boldsymbol{\nabla} u \cdot \boldsymbol{\nabla} \overline{v}\, d\Omega^e + \int_{\Omega^e} \left(\frac{\partial u}{\partial r} - iku \right) \overline{\left(\frac{\partial v}{\partial r} - ikv \right)}\, d\Omega^e \tag{2.9}$$

Two particular weights are of interest,

$$w(\boldsymbol{x}) = \begin{cases} 1 & \text{for} \quad r = |\boldsymbol{x}| \leq 1 \\ \dfrac{1}{r^2} & \text{for} \quad r = |\boldsymbol{x}| > 1 \end{cases}$$

and a "dual" weight

$$w^*(\boldsymbol{x}) = \begin{cases} 1 & \text{for} \quad r = |\boldsymbol{x}| \leq 1 \\ r^2 & \text{for} \quad r = |\boldsymbol{x}| > 1 \end{cases}$$

The variational formulation reads now as follows

$$\begin{cases} \text{Find } u \in H^+_{1,w}(\Omega^e) \text{ such that} \\ \displaystyle\int_{\Omega^e} \boldsymbol{\nabla} u \cdot \boldsymbol{\nabla} \overline{v} \, d\Omega^e - k^2 \int_{\Omega^e} u \, \overline{v} \, d\Omega^e = \int_{\partial\Omega^e} \tilde{g} \, \overline{v} \, dS \quad \forall \, v \in H^+_{1,w^*}(\Omega^e) \end{cases} \tag{2.10}$$

Remarks:

1. As for the sphere problem, the proposed variational formulation corresponds to an extension of the operator setting of Leis [16], where the domain of the operator is restricted to a *subspace* of $H^+_{1,w}(\Omega^e)$ consisting of all functions for which the (Helmholtz) operator value is in the weighted $L^2_{w^*}(\Omega^e)$ space. With these assumptions, Leis proves the uniqueness and existence of solutions, showing that the resulting operator is *bounded below* with a constant *locally* independent of wave number k.

2. Essentially the same formulation has been proposed in [1], [5], [6] and [13].

The Burnett formulation is introduced in the same way as for the sphere problem. Both solution u and test function v are represented outside of the unit sphere in the form

$$\begin{aligned} u(r,\theta,\phi) &= \frac{\exp(ikr)}{r} u_0(\theta,\phi) + U(r,\theta,\phi) \\ v(r,\theta,\phi) &= \frac{\exp(ikr)}{r} v_0(\theta,\phi) + V(r,\theta,\phi) \end{aligned} \tag{2.11}$$

where r, θ, ϕ are spherical coordinates, where functions $u_0(\theta,\phi)$ and $v_0(\theta,\phi)$ denote the radiation patterns, and functions $U(r,\theta,\phi)$, $V(r,\theta,\phi)$ are from $H^1(\Omega^e_s)$, i.e. both U, V and their gradients $\boldsymbol{\nabla} U$, $\boldsymbol{\nabla} V$ are square-integrable. Function u of this form satisfies *automatically* the Sommerfeld radiation condition. Upon substituting formulas (2.11) into (2.4) and cancelling out terms involving the radiation patterns, one can pass to the limit with $\gamma \to \infty$. Contrary to the weighted spaces formulation, the integral over S_γ involving the radiation patterns *will not* vanish in the limit, and the integral over the exterior domain Ω^e is to be understood in the CPV sense described above.

2.4 Separation of Variables in Ω_s^e and the Asymptotic Form of the Solution

Using the classical separation of variables approach, one arrives at the following form of the solution, valid outside the truncating unit sphere.

$$u(r,\theta,\phi) = \sum_{n=0}^{\infty}\sum_{m=0}^{n} h_n(kr)P_n^m(\cos\theta)\left(A_{nm}\cos(m\phi) + B_{nm}\sin(m\phi)\right) \tag{2.12}$$

where $P_n^m(\cos\theta)$ are the Legendre functions.

Using the representation from [17], the spherical Hankel functions of the first kind may be represented as

$$h_n(kr) = \frac{1}{kr}\exp\left(-i\frac{\pi}{2}(n+1) + ikr\right)\sum_{m=0}^{n} i^m\left(n+\frac{1}{2},m\right)(2kr)^{-m} \tag{2.13}$$

with

$$\left(n+\frac{1}{2},m\right) = \begin{cases} 1 & m=0 \\ \prod_{k=1}^{m}(n+k)\cdot\prod_{k=1}^{m}\frac{(n-m+k)}{k} & m\geq 1 \end{cases}$$

The terms can be reordered to obtain

$$h_n(kr) = \sum_{m=0}^{n}\frac{\exp(ikr)}{r^{m+1}}\frac{\exp\left(-i\frac{\pi}{2}(n+1)\right)}{k(2k)^m}i^m\left(n+\frac{1}{2},m\right) \tag{2.14}$$

2.5 Definition of the *hp*-Infinite Element

The following shape functions in the radial direction were used for the sphere problem in [8]:
the trial functions

$$\psi_j(r) = \frac{\exp(ikr)}{r^j}, \qquad j\geq 1 \tag{2.15}$$

the test functions

$$\tilde{\psi}_j(r) = \frac{\exp(ikr)}{r^{j+2}}, \qquad j\geq 1 \tag{2.16}$$

Note the different powers of r in the denominators. The use of the sesquilinear formulation eliminated the need of integration of the oscillatory component $\exp(ikr)$.

The infinite element shape functions were then defined as tensor products of 2D finite element shape functions and the functions introduced in (2.15) and (2.16) respectively, i.e. a typical infinite element trial shape function $N_l(r,\boldsymbol{x})$ was given by

$$N_l(r,\boldsymbol{x}) = N_{l(i,j)}(r,\boldsymbol{x}) = \psi_j(r)\cdot\varphi_i(\boldsymbol{x}), \qquad r>1,\ \boldsymbol{x}\in\Gamma_s \tag{2.17}$$

In order to minimize the interaction with finite elements within truncated domain Ω_s, the IE trial shape functions are now modified as follows

$$N_{l(i,j)}(r,\boldsymbol{x}) = \begin{cases} \exp(-ik)\ \psi_j(r)\ \varphi_i(\boldsymbol{x}) & j=1,\ r>1,\ \boldsymbol{x}\in\Gamma_s \\ \exp(-ik)\ (\psi_j(r)-\psi_1(r))\ \varphi_i(\boldsymbol{x}) & j\geq 2,\ r>1,\ \boldsymbol{x}\in\Gamma_s \end{cases} \tag{2.18}$$

with an identical modification for the test functions. In this way, all the shape functions corresponding to $j \geq 2$ will contribute to basis functions with supports outside of the unit sphere only. Inclusion of the exponential factor $\exp(-ik)$ in the new definition forces the infinite element shape functions to coincide with the standard 2D *hp* shape functions on the surface of the sphere.

2.6 3D *hp*-Adaptive FE Discretization

The domain Ω_s in between the scatterer and the truncating sphere is discretized using (triangular) prismatic *hp*-elements introduced in [10].

Master element. The master prismatic element, shown in Figure 2, consists of six vertex nodes and fifteen *higher-order* nodes: nine *mid-edge*, two *mid-base*, three *mid-side* and one *middle* node. The corresponding shape functions are tensor products of the 2D triangle shape functions $\chi_i(\xi_1,\xi_2)$ discussed in [12] and 1D *incremental* shape functions $\chi_j(\xi_3)$

$$\chi_k(\xi_1,\xi_2,\xi_3) = \chi_i(\xi_1,\xi_2)\cdot\chi_j(\xi_3), \quad k=k(i,j) \tag{2.19}$$

For $j=1,2$, functions $\chi_j(\xi_3)$ are the regular linear shape functions. Given a particular order of approximation q in the "vertical" (ξ_3) direction, functions $\chi_j(\xi_3)$, $j=1,\ldots,q-1$, coincide with the regular 1D Lagrange shape functions of order q, vanishing at the endpoints.

Consequently, the mid-side and the middle node have two corresponding orders of approximations: a horizontal p and a vertical order q. For that reason, we frequently talk about the *hpq* FE approximations. For all details concerning the definition of the master element we refer to [10].

Geometry representation. The domain Ω_s is viewed as a union of disjoint blocks. For each of the three considered configurations, the topology is the same, and the domain is covered with 8 triangular, and 8 rectangular prisms. The bottom base of each of the prisms coincides with a triangle or a rectangle on the scatterer and the top base lies on the unit sphere. The concept is illustrated in Figure 3.

Each of the prisms is viewed as the image of a corresponding standard master triangular or rectangular prism. The triangles and rectangles are parametrized using explicit

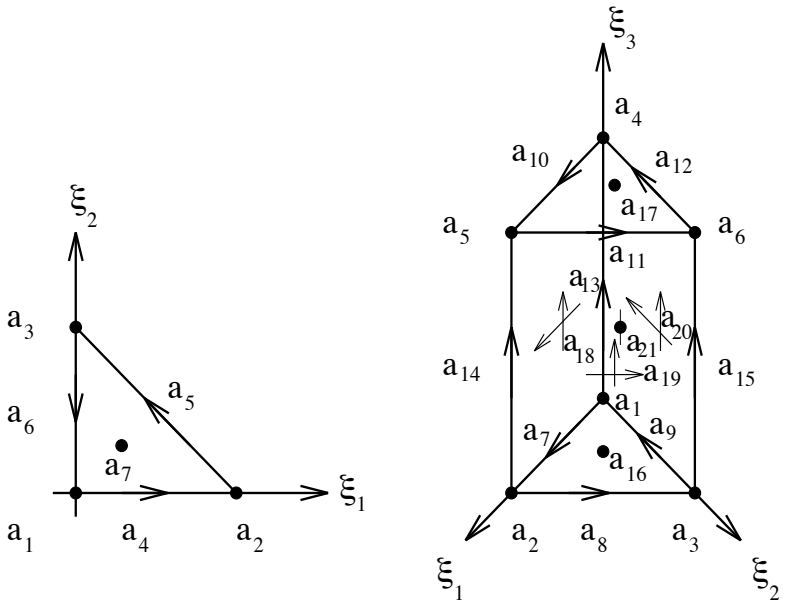

Figure 2: Master triangle and master prism

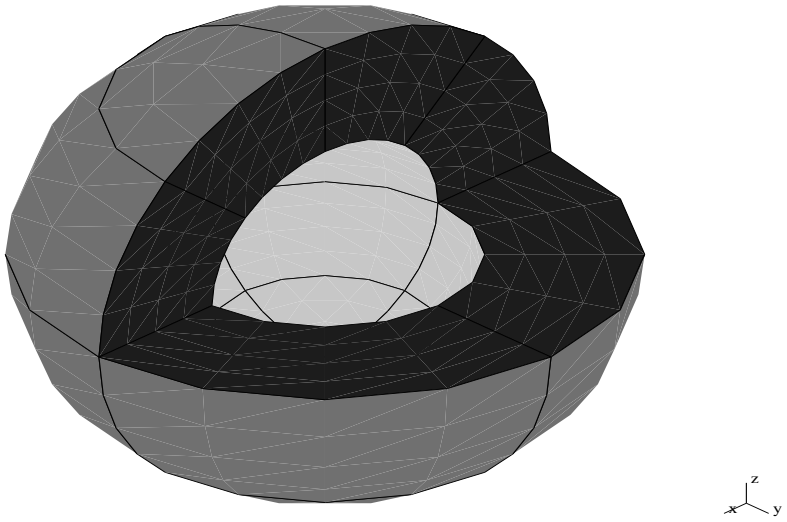

Figure 3: Geometry model for a sphere within the unit sphere. Three quarters of the model are displayed.

parametrizations discussed in [11] and a linear parametrization is used in the "vertical" direction. For all the details concerning the geometric modeling, we refer to [11].

The initial mesh is generated by using the idea of an *algebraic mesh generator* and *hp*-interpolation. Given, for the reference prism numbers n and l of divisions in the "horizontal" and "vertical" directions respectively, (compatible for neighboring elements, the initial mesh is always regular), the reference blocks are covered with uniform, regular grids consisting of elements $\tilde{K}$. By constructing a composition of the standard affine map $\boldsymbol{\eta}$ transforming the master element $\hat{K}$ onto element $\tilde{K}$ and the (restriction of) the block parametrization $\boldsymbol{x}_b$, a map is constructed from the master element $\hat{K}$ onto a curvilinear element K, identified as the image of element $\tilde{K}$ under the particular parametrization $\boldsymbol{x}_b$.

$$K = \boldsymbol{x}(\hat{K}) = \boldsymbol{x}_b(\tilde{K})\,, \qquad \boldsymbol{x} = \boldsymbol{x}_b \circ \boldsymbol{\eta} \tag{2.20}$$

In principle, this map could be used directly to define the curvilinear element, i.e. in the element calculations. In practice, it is approximated using the idea of *isoparametric* approximation. More precisely, given a particular order of approximation for element K (may vary for different nodes), transformation $\boldsymbol{x}$ is replaced with its *hp-interpolation*.

The idea of the *hp*-interpolation follows from the convergence theory for *hp* approximations [3] and has been introduced in [18] (comp. also [7]). Roughly speaking, the *hp*-interpolation combines the classical interpolation for vertex nodes with local H_0^1-projections for higher-order nodes. Given a sufficiently regular function, the corresponding *hp*-interpolant exhibits *the same* orders of convergence (in terms of both h and p) as the corresponding global H_0^1-projection (solution to the Laplace equation with Dirichlet boundary conditions imposed using the H_0^1 projection on the boundary). The same *hp*-interpolation technique is used during mesh refinements.

A typical initial FE mesh for a spherical scatterer with radius 0.5, located inside of the unit sphere, is shown in Figure 4. In the example there are 2 layers of 3D finite elements with 24 elements per layer, $p = 4$, $q = 2$ and 24 elements on the surface of the unit sphere representing 24 infinite elements.

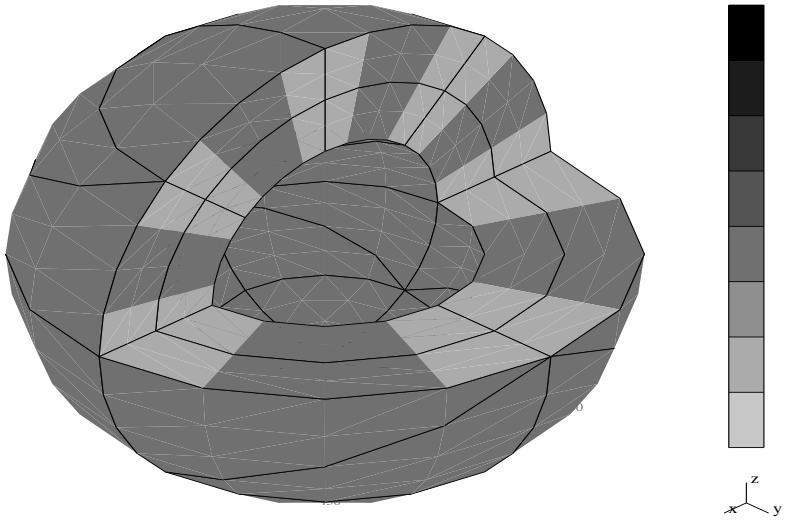

Figure 4: Initial Finite Element Mesh for the rigid scattering on a sphere within the unit sphere with p=4, q=2, 2 layers of finite elements. Three quarters of the mesh are displayed.

3 Numerical Experiments

3.1 Implementation Details for the Helmholtz Equation

The integration of the exponential terms in the radial direction for the infinite element involves terms of the following type

$$\int_1^\infty r^2 \psi_j(r) \overline{\tilde{\psi}_{\tilde{j}}(r)}\, dr = \int_1^\infty r^2 \frac{\exp(ikr)}{r^j} \frac{\exp(-ikr)}{r^{\tilde{j}+2}}\, dr = \frac{1}{j+\tilde{j}-1} \tag{3.1}$$

$$\int_1^\infty \psi_j(r) \overline{\tilde{\psi}_{\tilde{j}}(r)}\, dr = \int_1^\infty \frac{\exp(ikr)}{r^j} \frac{\exp(-ikr)}{r^{\tilde{j}+2}}\, dr = \frac{1}{j+\tilde{j}+1} \tag{3.2}$$

$$\begin{aligned} \int_1^\infty r^2 \frac{\partial \psi_j(r)}{\partial r} \frac{\partial \overline{\tilde{\psi}_{\tilde{j}}(r)}}{\partial r} dr &= \int_1^\infty r^2 \left(ik \frac{\exp(ikr)}{r^j} - j \frac{\exp(ikr)}{r^{j+1}} \right) \\ &\quad \cdot \left(-ik \frac{\exp(-ikr)}{r^{\tilde{j}+2}} - (\tilde{j}+2) \frac{\exp(-ikr)}{r^{\tilde{j}+3}} \right) dr \\ &= \frac{k^2}{j+\tilde{j}-1} + \frac{ik(j-(\tilde{j}+2))}{j+\tilde{j}} + \frac{j(\tilde{j}+2)}{j+\tilde{j}+1} \end{aligned} \tag{3.3}$$

Having these integrals computed ahead of time the calculation of the infinite element stiffness matrices is straightforward and reduces to standard 2D FE-like calculations.

The computation of the 3D finite element stiffness matrices is also standard and the element contributions are then assembled by a frontal solver adapted to handle complex matrices. The element load vector is calculated similarly.

It should be noted that the final global stiffness matrix is not symmetric.

3.2 Scattering of a Plane Wave by a Rigid Sphere with Radius 0.5

The derivation of the scattered wave on a rigid sphere with radius 0.5 corresponding to an incident plane wave can be found, e.g. in [13]. The final form of the scattered wave p^s is

$$p^s = \sum_{n=0}^{\infty} h_n(kr) P_n^m(\cos\theta) A_n \tag{3.4}$$

with A_n given by

$$A_n = \frac{-P_{inc}(2n+1)i^n \left.\frac{\partial j_n(kr)}{\partial r}\right|_{r=0.5}}{\left.\frac{\partial h_n(kr)}{\partial r}\right|_{r=0.5}} \qquad \forall \quad n \geq 1. \tag{3.5}$$

3.3 Error Calculations

Consistent with the variational formulation, the error between the numerical and the exact solution is measured in the weighted H^1-norm in Ω^e, where

$$\|u - u_h\|^2_{1,\Omega^e} = \|u - u_h\|^2_{1,\Omega_s^e} + \|u - u_h\|^2_{1,\Omega_s} \tag{3.6}$$

with

$$\|u - u_h\|^2_{1,\Omega_s^e} = \int_{\Omega_s^e} \frac{1}{r^2} |u - u_h|^2 \, d\Omega_s^e + \int_{\Omega_s^e} \frac{1}{r^2} \left|\boldsymbol{\nabla}(u - u_h)\right|^2 \, d\Omega_s^e \tag{3.7}$$

and

$$\|u - u_h\|^2_{1,\Omega_s} = \int_{\Omega_s} |u - u_h|^2 \, d\Omega_s + \int_{\Omega_s} \left|\boldsymbol{\nabla}(u - u_h)\right|^2 \, d\Omega_s \tag{3.8}$$

The exact solution u for the rigid scattering of a sphere with radius 0.5 is given by (3.4) and the numerical solution in Ω_s^e can be represented in the form

$$u_h(r, \boldsymbol{x}) = \sum_{j=1}^{N} \sum_{i=1}^{M} u_{ji} N_{l(i,j)}(r, \boldsymbol{x}) \qquad \boldsymbol{x} \in \Gamma_s, \ r > 1 \tag{3.9}$$

where $N_{l(i,j)}$ represent *hp*-basis functions of the IE and u_{ji} denote the corresponding degrees of freedom. In Ω_s the numerical solution is given by

$$u_h = \sum_{i=1}^{nrdof} u_i \varphi_i \tag{3.10}$$

where $\varphi_i,\ i = 1, \ldots, nrdof$, represents the 3D finite element shape functions. The evaluation of $\|u - u_h\|^2_{1,\Omega_s}$ follows the standard FE computations. For the computation of the error $\|u - u_h\|^2_{1,\Omega_s^e}$, we refer to [13].
Remarks:

1. In the error computation the term corresponding to the Sommerfeld radiation condition is neglected; compare with (2.9).

2. The integrals in the radial direction in (3.7) are integrated exactly and a higher order Gauss rule is used for the integration over $\partial\Omega_s^e$. Similarly, a higher order Gauss rule is used for the evaluation of (3.8).

3.4 Choice of an Initial FE Mesh

Due to the oscillatory character of the solution, choosing an arbitrary initial FE/IE mesh may not lead to any reasonable numerical solution. In particular, the initial mesh has to be chosen dependently on the wave number k and the prescribed Neumann boundary condition data on the surface of the scatterer.

For the sphere problem it is possible to compute the *best approximation error* in Ω_s

$$\inf_{u_h \in V_h(\Omega_s)} \|u - u_h\|_{H^1_w(\Omega_s)} \tag{3.11}$$

where $V_h(\Omega_s) \subset H^1(\Omega_s)$ is the finite dimensional FE subspace of the Sobolev space $H^1(\Omega_s)$.
The minimization problem

$$\begin{cases} \text{Find } u_h^{ba} \in V_h(\Omega_s) \text{ such that} \\ \|u - u_h^{ba}\|_{H^1(\Omega_s)} = \inf\limits_{v_h \in V_h(\Omega_s)} \|u - v_h\|_{H^1(\Omega_s)} \end{cases} \tag{3.12}$$

is equivalent to the variational formulation

$$\begin{cases} \text{Find } u_h^{ba} \in V_h(\Omega_s) \quad \text{such that} \\ (u_h^{ba}, v_h)_{H^1(\Omega_s)} = (u, v_h)_{H^1(\Omega_s)} \qquad \forall\ v_h \in V_h(\Omega_s) \end{cases} \tag{3.13}$$

where $(u, v)_{H^1(\Omega_s)}$ is the H^1-inner product

$$(u, v)_{H^1(\Omega_s)} = \int_{\Omega_s} \boldsymbol{\nabla} u \cdot \boldsymbol{\nabla} \overline{v} + u\overline{v} \, d\Omega_s \tag{3.14}$$

For a given wave number k and Neumann boundary condition data corresponding to an incident plane wave restricted to the surface of the scatterer, the sphere with radius 0.5, the exact solution u is given by (3.4). The best approximation error is then computed as

$$\|u - u_h^{ba}\|_{H^1_w(\Omega_s)} \tag{3.15}$$

Table 1 shows the best approximation error for an incident plane wave with wave number $k = 10$ for various meshes, depending on

- the polynomial degree in the angular ("horizontal") direction p
- the polynomial degree in the radial ("vertical") direction q
- the number of the layers of the 3D finite elements l
- the number of the 3D finite elements per layer n

3.5 Convergence Rates

The following discussion presents convergence rates for different examples of finite-infinite element meshes. It focuses on the question of, how the number of the shape functions in the radial direction affects the approximation of the exact solution.

A realistic example is the plane wave problem, described in Section 3.2. The assumed incident plane wave generates a scattered plane wave, which has an infinite number of terms in the radial direction. In the computations this series is truncated after 10 terms.

Figure 5 shows the p-convergence rates for wave number $k = 2$ with different q and number of dof in radial direction. Figures 6 - 7 display the p-convergence rates for wave number $k = 10$.

One does not observe the exponential shape of the p-convergence rates plots as it might be expected. The reason for this behavior is that only one parameter, the polynomial degree p in the angular direction, is varied, and that the quality of the approximation cannot be improved, if, for example, the discretization in the radial direction is not fine enough. In summary, these graphs clearly indicate, that p-, q- and/or h-mesh refinements for the 3D-FE mesh have to be performed simultaneously, along with a sufficient number of terms used in the radial direction of the infinite element.

p	q	l	n	$\frac{\|u-u_h^{ba}\|_{H^1_w(\Omega_s)}}{\|u\|_{H^1_w(\Omega_s)}}$	$\frac{\|u-u_h^{ba}\|_{L^2(\Omega_s)}}{\|u\|_{L^2(\Omega_s)}}$
5	2	2	96	12.08	4.50
5	2	1	96	37.89	24.99
5	2	2	24	12.21	4.53
5	2	1	24	37.94	25.00
5	3	2	96	2.84	0.72
5	3	1	96	15.47	7.90
5	3	3	24	2.09	0.55
5	3	2	24	3.33	0.88
5	3	1	24	15.58	7.92
4	2	4	96	3.59	0.69
4	2	3	96	5.93	1.5
4	2	2	96	12.11	4.50
4	2	1	96	37.90	24.99
4	2	5	24	4.75	1.47
4	2	4	24	5.41	1.58
4	2	3	24	7.19	2.06
4	2	2	24	12.77	4.72
4	2	1	24	38.10	25.01
4	3	4	96	1.16	0.21
4	3	3	96	1.45	0.26
4	3	2	96	2.98	0.74
4	3	1	96	15.51	7.90
4	3	5	24	4.19	1.43
4	3	4	24	4.21	1.43
4	3	3	24	4.30	1.44
4	3	2	24	5.03	1.60
4	3	1	24	16.02	8.02
3	2	5	96	3.61	0.79
3	2	4	96	4.44	0.97
3	2	3	96	6.48	1.65
3	2	2	96	12.39	4.56
3	2	1	96	37.98	24.99

Table 1: Best approximation error in Ω_s in percent measured in the H^1- and L^2-norm

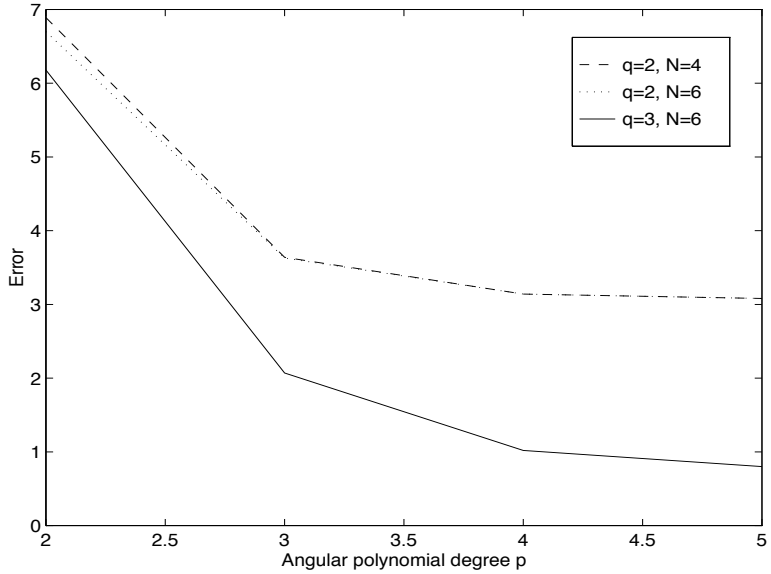

Figure 5: Scattering of a plane wave on a rigid sphere. Experimental p-convergence rates with 48 3D finite elements and 24 infinite elements with N terms in the radial direction for the Helmholtz equation with $k = 2$.

It is evident that the investigated finite-infinite element method works well for a smaller wave number, i.e. $k = 2$, but, at the same time, the quality of the approximation decreases as the wave number is increased. Nevertheless, the results show that the method is reliable for higher wave numbers as well, provided sufficiently fine meshes are used. The best approximation error results in Tables 1 indicate that the cost will increase with larger wave numbers. Recent results by Ihlenburg [15] on the so called polution error for the Helmholtz equation with high wave numbers imply that the number of dof for a reliable numerical solution will be larger, compared with what follows from the best approximation error analysis.

3.6 Numerical Results for Other Geometries

In this section, numerical results for the rigid scattering on a (finite) cylinder and a (finite) cylinder with spherical incaps are presented. Both cylinders are contained within the unit sphere. The Neumann boundary condition on the surface of the scatterer corresponds to an incident plane wave.

The IEM is used to compute solutions for the rigid scattering on both cylinders with wave number $k = 1$ and 10. The finite element mesh contains three layers of finite

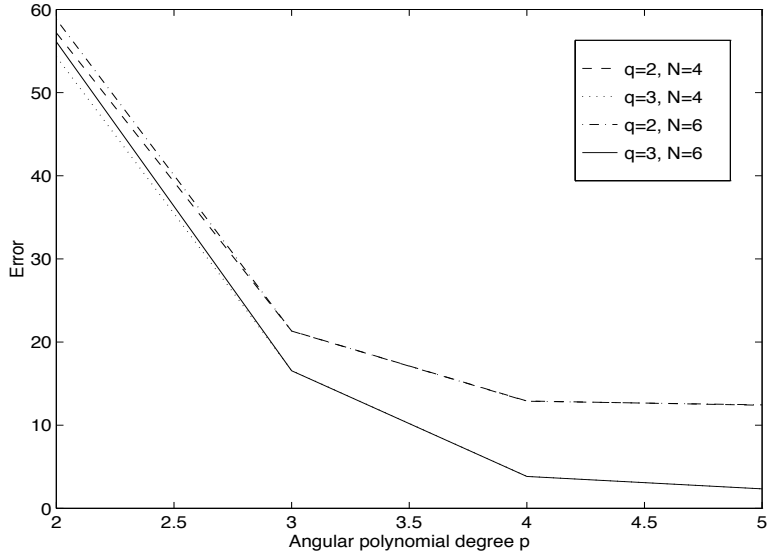

Figure 6: Scattering of a plane wave on a rigid sphere. Experimental p-convergence rates with 48 3D finite elements and 24 infinite elements with N terms in the radial direction for the Helmholtz equation with $k = 10$.

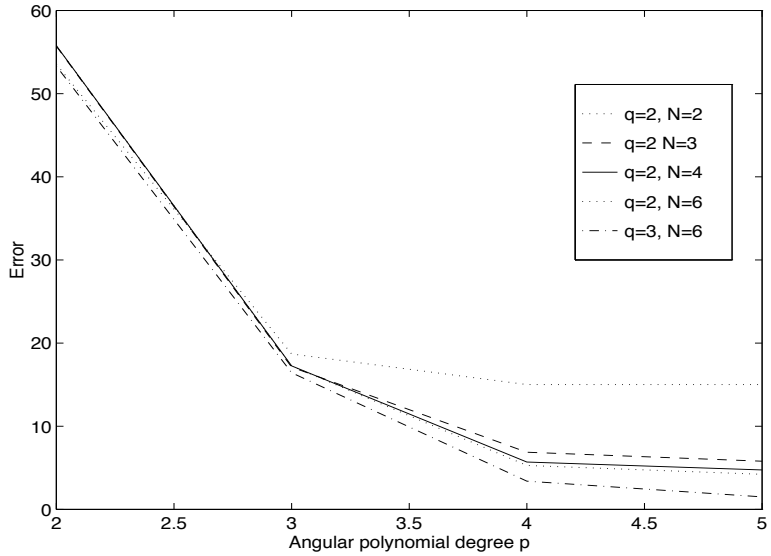

Figure 7: Scattering of a plane wave on a rigid sphere. Experimental p-convergence rates with 72 3D finite elements and 24 infinite elements with N terms in the radial direction for the Helmholtz equation with $k = 10$.

elements with 216 finite elements per layer, $p = 3$ and $q = 2$. There are 216 infinite elements with $p = 3$ and 6 radial shape functions. Altogether, 864 elements are used.

Computing the numerical solution with the coupled FE/IE methodology takes fifteen to twenty minutes on a DEC 3000 workstation. Numerical solutions obtained by the BEM are only presented for $k = 1$, since the workstation was not capable of computing solutions for $k >> 1$, due to the memory and CPU demands for higher wave numbers of the particular BEM implementation.

From Figures 10, 11 and 13, 14 we see that the imaginary components of the total pressure are in good agreement. The real component obtained by the BEM in Figure 9 does not appear to be as good as the real component obtained by the FEM/IEM in Figure 8. Finally, the obtained absolut value of the total pressure for wave number $k = 10$ is displayed in Figures 12 and 15.

4 Adaptive *hp*-Mesh Refinement

This section describes a strategy for performing automated adaptive *hp*-mesh refinements. We intend to show only that the methodology of coupled finite/infinite element approximations can be embedded into the usual adaptive mesh refinement procedures. A rigorous error estimator for the exterior Helmholtz problem has not been developed and for the sake of simplicity of the implementation, only a very crude error indicator has been used to show the possibility of using the *hp*-mesh refinements in context of the coupled finite/infinite element methodology. The error indicator decribed in the next section will eventually have to be replaced with a more sophisticated, appropriate error estimator for the exterior Helmholtz problem.

4.1 An Error Indicator on Ω_s

The error indicator compares the numerical solution pointwise on two different meshes and provides an error indication for each finite element. More precisely, the numerical solution u_h^i is computed on an initial mesh and then compared to the numerical solution u_h^r obtained on a refined mesh. The difference between u_h^i and u_h^r, measured in the L^∞-norm over each finite element Ω_l, serves as the error indicator η_l, i.e.

$$\eta_l = \|u_h^i - u_h^r\|_{L^\infty(\Omega_l)} \tag{4.1}$$

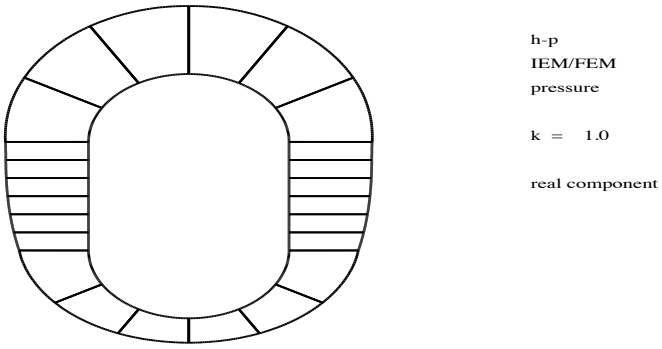

Figure 8: FEM/IEM. Scattering of a plane wave on a rigid cylinder with spherical incaps, $k = 1$. Real part of the scattered pressure obtained with a mesh of 648 3D finite elements ($l = 3$, $n = 216$) of order $p = 3$, $q = 2$, and 216 infinite elements with 6 terms in the radial direction

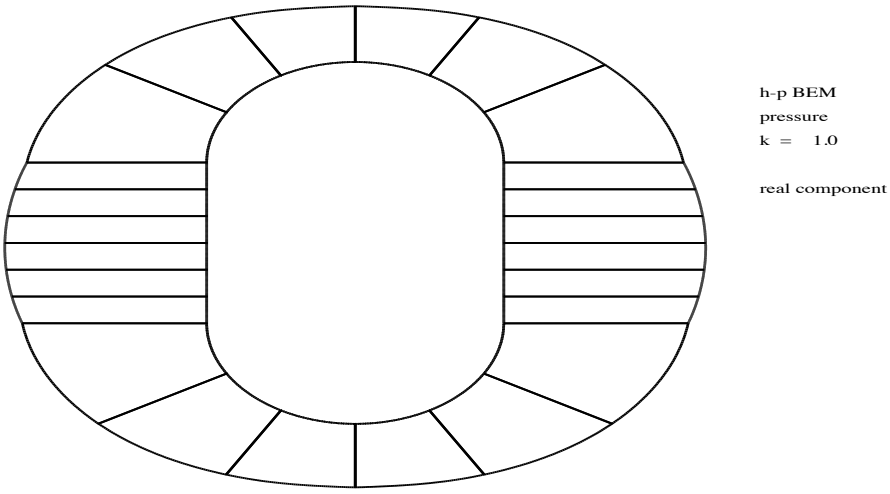

Figure 9: BEM. Scattering of a plane wave on a rigid cylinder with spherical incaps, $k = 1$. Real part of the scattered pressure obtained with a mesh of 216 2D finite elements of order $p = 3$

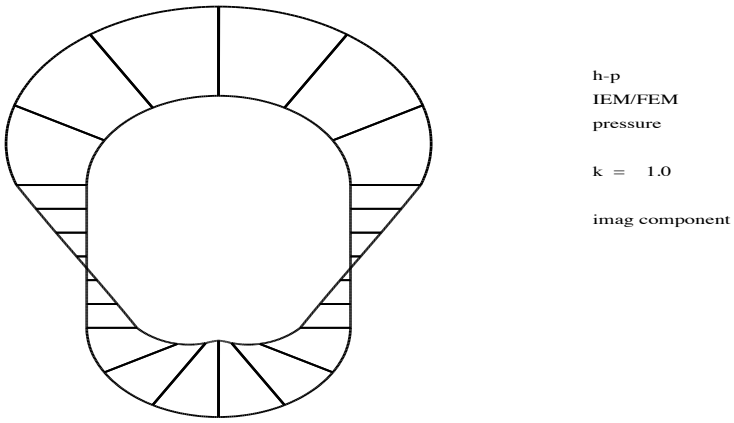

Figure 10: FEM/IEM. Scattering of a plane wave on a rigid cylinder with spherical incaps, $k = 1$. Imaginary part of the scattered pressure obtained with a mesh of 648 3D finite elements ($l = 3$, $n = 216$) of order $p = 3$, $q = 2$, and 216 infinite elements with 6 terms in the radial direction

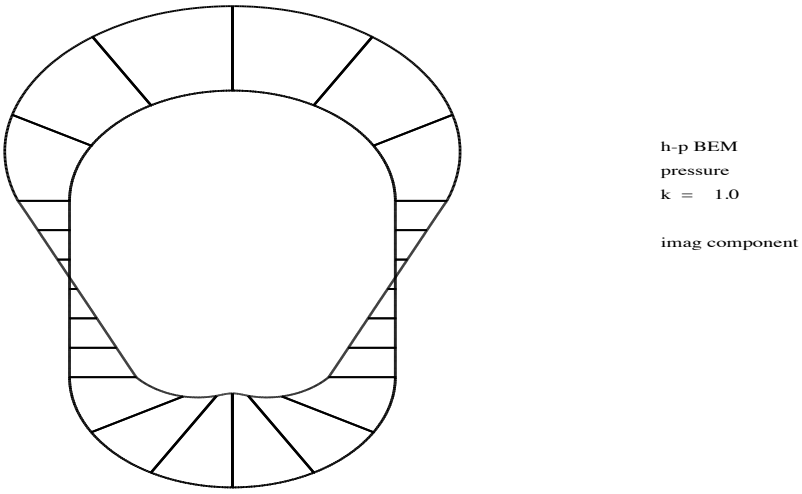

Figure 11: BEM. Scattering of a plane wave on a rigid cylinder with spherical incaps, $k = 1$. Imaginary part of the scattered pressure obtained with a mesh of 216 2D finite elements of order $p = 3$

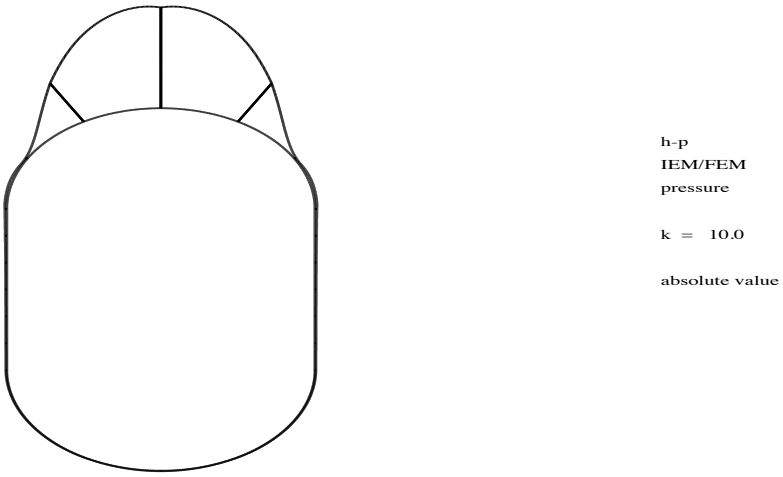

Figure 12: FEM/IEM. Scattering of a plane wave on a rigid cylinder with spherical incaps, $k = 10$. Absolute value of the scattered pressure obtained with a mesh of 648 3D finite elements ($l = 3$, $n = 216$) of order $p = 3$, $q = 2$, and 216 infinite elements with 6 terms in the radial direction

In practice, η_l is obtained by comparing the values of u_h^i and u_h^r at the corresponding Gauss points in each finite element Ω_l, that is

$$\eta_l = \max_{\boldsymbol{x}^{gp}} \left| u_h^i(\boldsymbol{x}^{gp}) - u_h^r(\boldsymbol{x}^{gp}) \right| \qquad \forall \text{ Gauss point } \boldsymbol{x}^{gp} \in \Omega_l \tag{4.2}$$

4.2 An Adaptive Mesh Refinement Strategy

The following adaptive mesh refinement strategy, based on the error indicator above, intends to illustrate only the possibility of changing both p and h, to obtain a non uniform hp-finite-infinite element mesh. The error indicator, given in the previous section, is computed for every 3D FE, after solving the scattering problem using the FE-IE methodology. Each element Ω_l, for which the relative error indicator η_l^r is greater than a treshhold value τ, will be refined, i.e. if

$$\eta_l^r = \frac{\eta_l}{\eta_t} > \tau \tag{4.3}$$

where η_t denotes the maximum element error indicator over the whole mesh. The compatibility between the FE and IE approximations is enforced by refining infinite elements

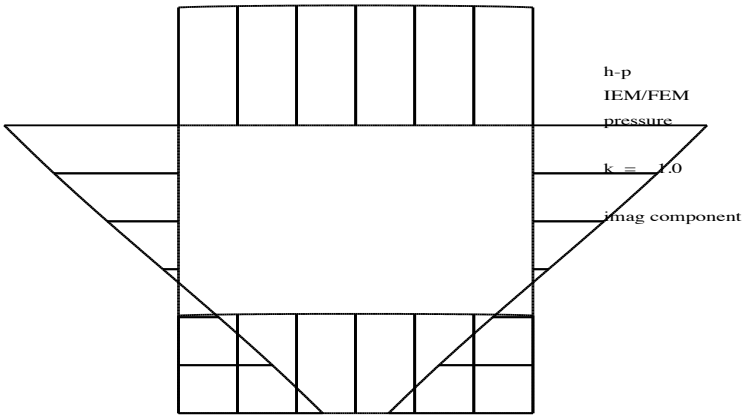

Figure 13: FEM/IEM. Scattering of a plane wave on a rigid cylinder, $k = 1$. Imaginary part of the scattered pressure obtained with a mesh of 648 3D finite elements ($l = 3$, $n = 216$) of order $p = 3$, $q = 2$, and 216 infinite elements with 6 terms in the radial direction

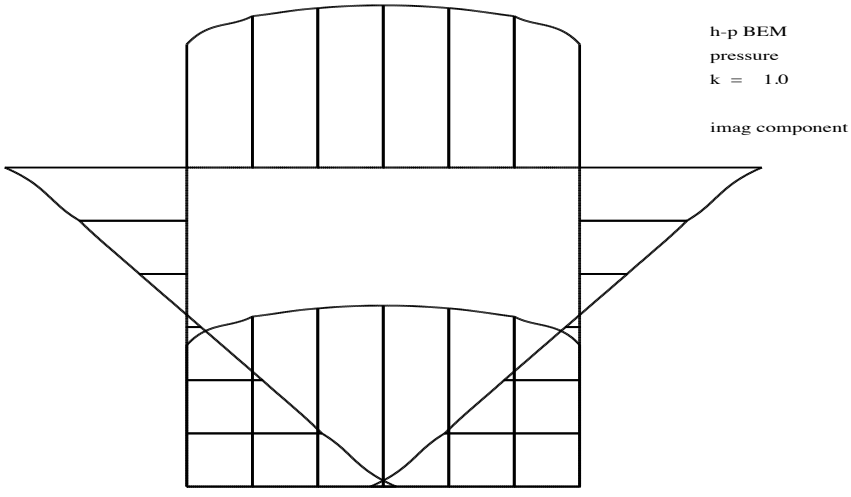

Figure 14: BEM. Scattering of a plane wave on a rigid cylinder, $k = 1$. Imaginary part of the scattered pressure obtained with a mesh of 216 2D finite elements of order $p = 3$

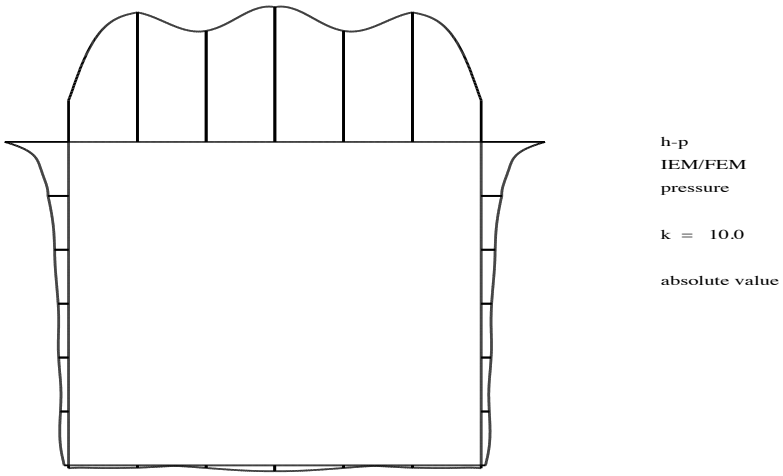

Figure 15: FEM/IEM. Scattering of a plane wave on a rigid cylinder, $k = 10$. Absolute value of the scattered pressure obtained with a mesh of 648 3D finite elements ($l = 3$, $n = 216$) of order $p = 3$, $q = 2$, and 216 infinite elements with 6 terms in the radial direction

adjacent to the refined finite elements. This means that an enrichement of the polynomial degree in the angular direction of the 3D FE or/and the $h4$-refinement of the 3D FE will also be carried out for the adjacent IE.

The scattering problem is solved on the refined mesh, and the error indicators are calculated again, with the whole procedure repeated. More precisely, the following algorithm has been used.

1. Compute the numerical solution on an initial mesh.
2. Perform a uniform p-refinement.
3. Compute the numerical solution on the refined mesh.
4. Compute the error indicator using the numerical solutions obtained in steps 1 and 3.
5. Perform a non-uniform p-refinement for elements, where $\eta_l^r > \tau$.
6. Compute the numerical solution on the non-uniform mesh.

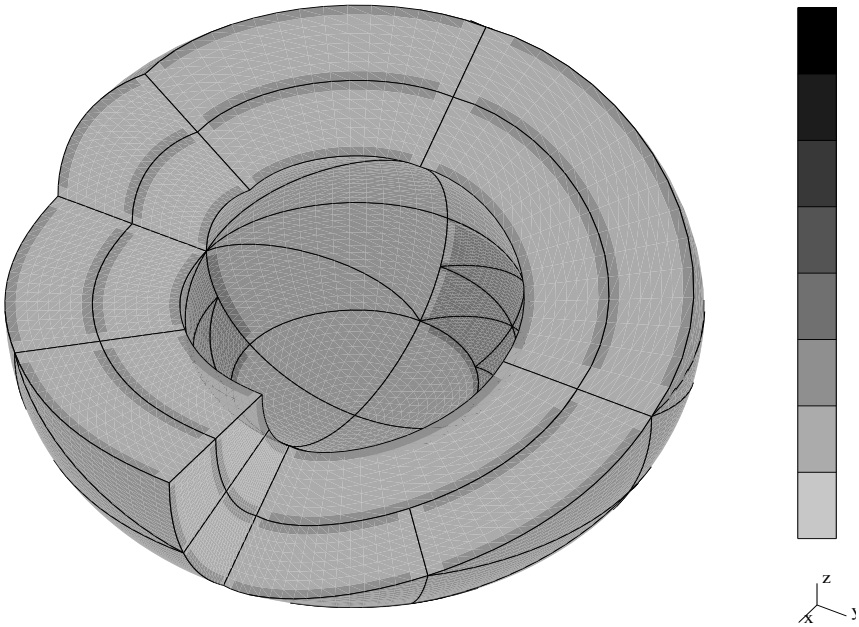

Figure 16: Adapted *hp*-finite-infinite element mesh.

7. Compute the error indicator using the numerical solutions obtained in steps 3 and 6.

8. Perform a non-uniform h-refinement for elements, where $\eta_l^r > \tau$.

9. Compute the numerical solution on the non-uniform *hp*-mesh.

Figure 16 shows a sample *hp*-finite element mesh obtained with the above procedure by assuming an incident plane wave with wave number $k = 5$ and using for the initial mesh: $N = 6$, i.e. six shape functions in the radial direction, $q = 2$ for the polynomial degree in the radial direction of the finite elements, $p = 2$ for the polynomial degree in the angular direction, and 2 layers of 3D finite elements with 24 elements per layer, i.e. there are also 24 infinite elements present. The value for τ is selected as $\tau = 3.5\%$.

5 Conclusions

The work reports on numerical experiments on *hp*-adaptive, coupled IE/FE discretizations for the 3D Helmholtz equation in exterior domains of arbitrary shape. The IE/FE

approximation presents a challenging alternative not only for the traditional boundary elements (BE) but also for the formulations based on various implementations of the so called Dirichlet-to-Neumann (DtN) operator, see eg. [14].

Contrary to the BE and DtN methods, the IE approximation *is local* and can be easily built into any FE code using standard C^0 elements, including the *hp*-adaptive FE discretizations.

The presented numerical results were confined to three cases:

- a sphere within the unit sphere,
- a (finite) cylinder within the unit sphere,
- a (finite) cylinder with spherical incaps within the unit sphere.

The sphere problem admits an exact solution and was the basis for a numerical convergence study of the coupled FEM/IEM. In the remaining two cases the IE/FE solutions were compared with numerical solutions obtained using the BE method presented in [9]. The presented numerical evidence indicates that the method converges. Further, the particular FEM/IEM is more efficient then the particular BEM implementation that was used. It also seems that the FEM/IEM methodology will be more efficient, even if the BEM will be specialized and tuned to the investigated problem.

In conclusion, several remarks suggest themselves:

1. The numerical results indicate that it is impossible, in general, to resolve the exterior boundary-value problem with a *fixed* number of approximating basis functions in the radial direction.
2. The method is stable for arbitrary *hp* FE discretizations in between the scatterer and the truncating surface, making the *hp* mesh adaptation possible.
3. In a more sophisticated implementation, the number of basis functions in the radial direction may vary from a node to a node and can be adapted during the solution.
4. Derivation of an *a-posteriori error estimator* indicating the error corresponding both to the 3D FE and the IE (in the radial direction) discretizations is necessary for a successful large scale implementation of the method.

Acknowledgement: The work has been supported by the Office of Naval Research under Contract N00014-89-J-1451.

References

[1] R. J. Astley, G. J. Macaulay and J. P. Coyette, "Mapped Wave Envelope Elements for Acoustical Radiation and Scattering", Journal of Sound and Vibration, vol. 170, no. 1, pp. 97-118, 1994.

[2] I. Babuska and J. J. Shirron, "Solution of Exterior Helmholtz Problems using Finite and Infinite Elements", Dissertation preprint

[3] I. Babuska and M. Suri, "The p and hp Versions of the Finite Element Method: Basic Principles and Properties", preprint 1994.

[4] D. S. Burnett, "A Three-Dimensional Acoustic Infinite Element Based on a Prolate Spheroidal Multipole Expansion", Journal of the Acoustical Society of America, vol. 96, pp. 2798-2816, 1994.

[5] L. Cremers, K. R. Fyfe and J. P. Coyette, "A Variable Order Infinite Acoustic Wave Envelope Element", Journal of Sound and Vibration, vol. 171, no. 4, pp. 483-508, 1994.

[6] L. Cremers and K. R. Fyfe, "On the use of Variable Order Infinite Wave Envelope Elements for Acoustic Radiation and Scattering", The Journal of the Acoustical Society of America, vol. 97, no. 4, pp. 2028-2040, 1995.

[7] L. Demkowicz and K. Banas, "3D hp Adaptive Package", SAM Report 2/1993, Section of Applied Mathematics, Cracow University of Technology, March 1993.

[8] L. Demkowicz and K. Gerdes, "Convergence of the Infinite Element Methods for the Helmholtz Equation", TICAM Report 95-07.

[9] L. Demkowicz and J. T. Oden, "Application of HP-Adaptive BE/FE Methods to Elastic Scattering", TICAM Report 94-15, December 1994.

[10] L. Demkowicz and J. T. Oden, "Recent Progress on Application of hp-Adaptive BE/FE Methods to Elastic Scattering", International Journal for Numerical Methods in Engineering, vol. 37, pp. 2893-2910, 1994.

[11] L. Demkowicz, A. Bajer and K. Banas, "Geometrical Modeling Package", TICAM Report 92-06, The University of Texas at Austin, August 1992.

[12] L. Demkowicz, A. Karafiat and J. T. Oden, "Solution of Elastic Scattering Problems in Linear Acoustics using hp Boundary Element Method", Computer Methods in Applied Mechanics and Engineering, vol. 101, pp. 251-282, 1992.

[13] K. Gerdes and L. Demkowicz, "Solutions of 3D-Laplace and Helmholtz Equations in Exterior Domains using hp Infinite Elements", accepted for publication in CMAME, October 1995.

[14] M.J. Grote and J.B. Keller, "On Nonreflecting Boundary Conditions", J. Comp. Phys. 122, 231-243, 1995.

[15] F. Ihlenburg and I. Babuska, "Finite Element Solution to the Helmholtz Equation with High Wave Number: Part 1: The h-version of the FEM", Computers & Mathematics with Applications, Vol. 30, No. 9, 9-37, 1995.

[16] R. Leis, Initial Boundary Value Problems in Mathematical Physics, Teubner, 1986.

[17] P. M. Morse and J. Feshbach, Methods of Theoretical Physics, vols 1 and 2, McGraw-Hill, New York, 1953.

[18] J. T. Oden, L. Demkowicz, W. Rachowicz and T. A. Westermann, "Towards a Universal $h-p$ Adaptive Finite Element Strategy, Part 2. *A Posteriori* Error Estimation", Comp. Meth. Appl. Meth. Eng., vol. 77, pp. 113-180, 1989.

[19] J. Sanchez Hubert and E. Sanchez Palencia, Vibration and Coupling of Continuous Systems, Springer Verlag, 1989.

Research Reports

No.	Authors	Title
96-21	K. Gerdes	Solution of the $3D$-Helmholtz equation in exterior domains of arbitrary shape using HP-finite infinite elements
96-20	C. Schwab, M. Suri, C. Xenophontos	The *hp* finite element method for problems in mechanics with boundary layers
96-19	C. Lage	The Application of Object Oriented Methods to Boundary Elements
96-18	R. Sperb	An alternative to Ewald sums. Part I: Identities for sums
96-17	M.D. Buhmann, Ch.A. Micchelli, A. Ron	Asymptotically Optimal Approximation and Numerical Solutions of Differential Equations
96-16	M.D. Buhmann, R. Fletcher	M.J.D. Powell's work in univariate and multivariate approximation theory and his contribution to optimization
96-15	W. Gautschi, J. Waldvogel	Contour Plots of Analytic Functions
96-14	R. Resch, F. Stenger, J. Waldvogel	Functional Equations Related to the Iteration of Functions
96-13	H. Forrer	Second Order Accurate Boundary Treatment for Cartesian Grid Methods
96-12	K. Gerdes, C. Schwab	Hierarchic models of Helmholtz problems on thin domains
96-11	K. Gerdes	The conjugated vs. the unconjugated infinite element method for the Helmholtz equation in exterior domains
96-10	J. Waldvogel	Symplectic Integrators for Hill's Lunar Problem
96-09	A.-T. Morel, M. Fey, J. Maurer	Multidimensional High Order Method of Transport for the Shallow Water Equations
96-08	A.-T. Morel	Multidimensional Scheme for the Shallow Water Equations
96-07	M. Feistauer, C. Schwab	On coupled problems for viscous flow in exterior domains
96-06	J.M. Melenk	A note on robust exponential convergence of finite element methods for problems with boundary layers
96-05	R. Bodenmann, H.J. Schroll	Higher order discretisation of initial-boundary value problems for mixed systems
96-04	H. Forrer	Boundary Treatment for a Cartesian Grid Method